

1 **Title page:**

2 **Very broadband strain-rate measurements along a submarine**
3 **fiber-optic cable off Cape Muroto, Nankai subduction zone,**
4 **Japan**

5 Author #1: Satoshi Ide, Department of Earth and Planetary Science, The University of

6 Tokyo, 7-3-1, Hongo, Bunkyo, Tokyo, 113-0033, Japan, ide@eps.s.u-tokyo.ac.jp

7 (corresponding author)

8 Author #2: Eiichiro Araki, Japan Agency for Marine Earth Science and Technology, 2-

9 15, Natsushima, Yokosuka, Kanagawa, 237-0061, araki@jamstec.go.jp

10 Author #3: Hiroyuki Matsumoto, Japan Agency for Marine Earth Science and

11 Technology, 2-15, Natsushima, Yokosuka, Kanagawa, 237-0061,

12 hmatsumoto@jamstec.go.jp

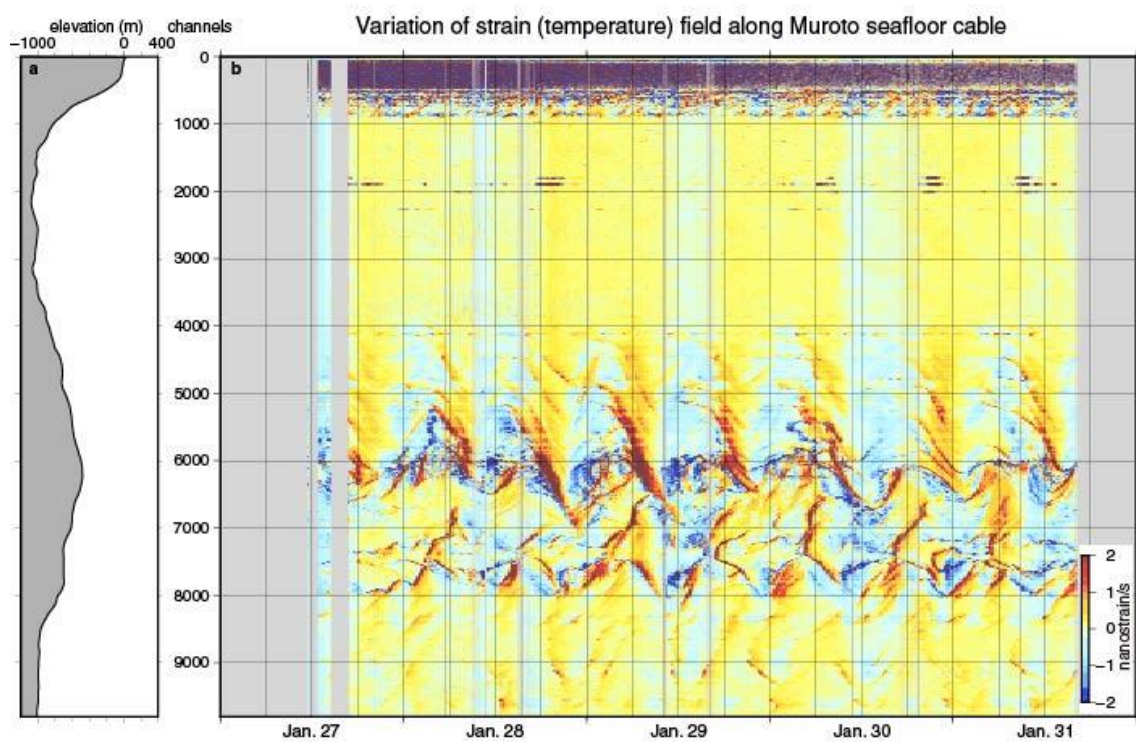
13

14 **Abstract**

15 Distributed acoustic sensing (DAS) is a new method that measures the strain change
16 along a fiber-optic cable and has emerged as a promising geophysical application across
17 a wide range of research and monitoring. Here we present the results of DAS
18 observations from an submarine cable offshore Cape Muroto, Nankai subduction zone,
19 western Japan. The observed signal amplitude varies widely among the DAS channels,
20 even over short distances of only ~ 100 m, which is likely attributed to the differences in
21 cable-seafloor coupling due to complex bathymetry along the cable route. Nevertheless,
22 the noise levels at the well-coupled channels of DAS are almost comparable to those
23 observed at nearby permanent ocean-bottom seismometers. Many earthquakes were
24 observed during the five-day observation period, with the minimum and maximum
25 detectable events being a local M1.1 event 30–50 km from the cable and a teleseismic
26 Mw7.7 event that occurred in Cuba, respectively. Temperature appears to exert a greater
27 control on the DAS signal than real strain in the quasi-static, sub-seismic range. We
28 observed many rapid temperature change events migrating along the cable: a small
29 number of large migration events (up to 10 km in 6 hours) associated with rapid

30 temperature increases, and many small-scale events (both rising and falling
31 temperatures). These events may reflect deep-ocean water mixing processes that are the
32 result of ocean current–tidal interactions along an irregular seafloor boundary.

33



34

35

36 **Keywords**

37 Distributed Acoustic Sensing (DAS), submarine cable, earthquakes, broadband, strain,

38 temperature, ocean current, tide, mixing processes

39

40 **Main Text**

41 **Introduction**

42 Distributed acoustic sensing (DAS) is a new geophysical imaging technique that
43 measures the ground strain (or strain rate) along a fiber-optic cable, using variations in
44 the phase-coherent Rayleigh backscattering that are generated by a sequence of laser
45 pulses (e.g. Hartog, 2017; Lindsey et al., 2020). Although DAS was originally
46 developed for the oil and gas industry, it has since been utilized to address a wide range
47 of seismological research topics (e.g., Zhan, 2020). It is a relatively inexpensive way to
48 obtain spatially dense and temporally continuous measurements, when we can use fiber-
49 optic cables that have already been installed for communication purposes. We can
50 simultaneously measure the strain at many locations along the cable (meter-scale
51 intervals) at a high-sampling rate (~1000 samples per second (sps)) by simply attaching
52 an interrogator, which is a laser transmitter/receiver system, to one end of the cable. It
53 has been reported that the noise levels of the strain measurements are sufficiently small
54 to detect natural earthquakes (Lindsey et al., 2017). Wang et al. (2018) have
55 demonstrated the similarity between DAS and seismograph strain measurements, and

56 confirmed that the observed signal is axial strain along a fiber-optic cable in the
57 ordinary frequency range for seismic observations (i.e., several Hertz). At lower
58 frequencies, Ajo-Franklin et al. (2019) observed the surface waves from large
59 teleseismic earthquakes, and Lindsey et al. (2020) demonstrated how to convert DAS
60 records into velocity seismograms via a comparative analysis of DAS and broadband
61 seismometer signals. Further applications for subsurface structural investigations have
62 been proposed, such as receiver function (Yu et al., 2019) and H/V spectral ratio (Spica
63 et al., 2020a) analyses.

64 Ocean-bottom strain measurements are a promising research direction for future DAS
65 observations since the installation of conventional geophysical sensors is difficult, and
66 several studies have successfully installed DAS interrogators along submarine
67 communication cables. Williams et al. (2019) used a telecommunication cable at
68 shallow (<40 m) depths offshore Belgium, and analyzed the spectral features of the
69 ambient DAS signals. These signals mostly consisted of ocean surface gravity waves
70 and Scholte waves, which reflect solid earth–ocean coupling. They also observed the
71 seismic waves from a large (Mw 8.2) teleseismic (hypocentral distance of $\sim 150^\circ$)

72 earthquake, although no regional earthquakes were recorded due to the low seismicity.
73 Sladen et al. (2019) also utilized a telecommunication cable offshore France for DAS
74 observations to detect a small (M1.9) earthquake that occurred ~100 km from the cable.
75 Shinohara et al. (2019) and Spica et al. (2020b) used a fiber-optic cable that was
76 originally installed for ocean-bottom seismic sensors to monitor active seismicity
77 offshore Tohoku region, Japan. In addition to observation of many small earthquakes,
78 they showed that DAS observations could potentially resolve spatial heterogeneities in
79 the very shallow seismic structure along the cable. Some ocean sediments possess
80 shear-wave (S-wave) velocities as low as 300 m/s. Such fine imaging of the subsurface
81 structure would be quite difficult without dense observations, such as those acquired via
82 DAS.

83 Here we used a fiber-optic cable that was originally used for ocean-bottom seismic
84 observations off Cape Muroto, Nankai subduction zone, where the Philippine Sea Plate
85 is subducting beneath western Japan at 3–5 cm/yr. Many large (M8+) historical
86 earthquakes have occurred in this region at 100–200-year intervals; more than 70 years
87 have now passed since the last large event, the 1946 Nankai Earthquake; therefore,

88 various observation instruments have been installed in this region with the hope of
89 obtaining comprehensive observations of the next expected large earthquake. Our fiber-
90 optic cable was a part of such observation systems. Although the ambient seismicity in
91 this region is low compared with other regions in Japan, various types of slow
92 earthquake (e.g., Beroza and Ide, 2011; Obara and Kato, 2016), such as slow slip events
93 and tectonic tremors, occur frequently in the region. The relationship between slow and
94 large megathrust earthquakes is of great interests and the effectiveness of DAS
95 observations in detecting such phenomena is important to evaluate. Our temporary
96 observations confirm the feasibility of acquiring DAS observations for earthquake
97 detection and analysis. Furthermore, we also demonstrate the potential to investigate
98 deep-ocean water movement via DAS observations, since these observations mainly
99 record temperature changes in the quasi-static, sub-seismic frequency range.

100

101 **DAS observations and noise levels**

102 The Japan Agency for Marine Earth Science and Technology (JAMSTEC) developed
103 the Comprehensive Seafloor Monitoring System off Cape Muroto in 1997 (Momma et

104 al., 1997). A submarine cable with six single-mode fibers connects the land station and
105 ocean-bottom instruments (Figure 1). The total cable length is 120 km, with two ocean-
106 bottom seismometers deployed 70 and 100 km from the coast. The system was operated
107 for more than 20 years before being ceased in 2019. The cable was not covered by
108 sediments, except for a 2-km shallow section, at the time of installation; however, the
109 current status of the seafloor cable is unknown. We used a 50-km section of the cable
110 that extended from the coast for the DAS observation. No instruments are attached to
111 this section. Figure 1 shows the regional bathymetry and estimated cable route. The
112 bathymetry is complex in this region, and the cable extends to the south, passing across
113 the edge of Muroto Basin and over Tosabae Ridge.

114 We acquired temporary DAS observations during the January 27–31, 2020 (JST) period
115 along this cable. We used a N5200A interrogator (AP Sensing), which was operated
116 with several different parameter settings. The most used parameter settings for our
117 observations were a 500-sps temporal sampling rate, 5.10-m spatial sampling interval,
118 and 40.4-m gauge length. There were 9788 channels in the 50-km section of cable. The
119 size of the uncompressed records was ~1 TB/day, since the interrogator measured a 16-

120 bit recording of the differential strain (strain rate) at each channel.

121 The sensitivity of the 9788 channels to ground strain varied along the cable. Some

122 channels recorded almost nothing, even when clear seismic signals were recorded at

123 other channels. These insensitive channels recorded low levels of ambient noise that

124 corresponded to microseisms, which are discussed later in the text. We computed the

125 standard deviation of the strain rate using a 5-min interval for the entire observation

126 period to visualize the spatial heterogeneity of the channel sensitivity. Figure S1 shows

127 the median values of the standard deviations for the entire observation period. The

128 insensitive channels are those with very small standard deviations, which are supposed

129 to be “uncoupled” from the ocean bottom. The observed amplitudes at channels 0–500

130 (first 2.5 km of cable from the coast) were often near the maximum of the dynamic

131 range, and were likely saturated due to the skipping of some cycles, which made the

132 analysis difficult. At channels 500–2200, the standard deviations were generally small

133 with the exception of some channels, suggesting weak coupling. There were two

134 sections with large standard deviations: channels 2200–3000 (~4 km length) and

135 channels 3500–4000 (~2.5 km length). Above channel 4000, there were alternating

136 sections of coupled and uncoupled channels. For the channels that were far from the
137 coast, there was a smooth increase in the standard deviation with channel number. This
138 increase likely arose from the high noise levels due to the attenuation of the laser pulses.
139 We selected ten channels and computed their spectrograms, which consist of
140 periodograms of the strain rate at 5-min intervals for the entire observation period
141 (Figure S2). Two of the ten channels (6000 and 7510) are examples of uncoupled
142 channels, which only recorded small amplitudes during the entire observation period.
143 Figure 2 summarizes the median of the spectral amplitude (5-min interval) for the entire
144 observation period at these ten channels, together with the spectral amplitudes that were
145 estimated in a similar manner using the accelerations at several nearby seismic stations
146 (and their associated networks): MUTH and KTGH (Hi-net, a high-sensitivity seismic
147 network with short period (1 Hz) sensors); UMJF (F-net, a broadband seismic network);
148 and MRA04 and MRG29 (DONET2, an ocean-bottom network with broadband
149 sensors). All these seismic stations are maintained by the National Research Institute for
150 Earth Science and Disaster Resilience, and the data are publicly available.
151 The amplitudes of the acceleration spectra at the two DONET2 stations are $\sim 10^{-6}$

152 $\text{m/s}^2/\text{Hz}^{1/2}$ above 2 Hz, whereas those of the DAS strain rate spectra are ~ 1
153 $\text{nanostain/s}/\text{Hz}^{1/2}$. These two levels are comparable if we assume plane waves with a
154 velocity of ~ 1 km/s are producing this background noise (e.g., Benioff, 1935). A peak at
155 0.3–0.5 Hz is visible in both the DONET2 and DAS observations, suggesting that
156 similar ambient signals are being recorded above 0.1 Hz. This peak at 0.3–0.5 Hz is
157 common in broadband ocean-bottom seismic observations (e.g., Araki et al., 2004;
158 Suetsugu and Shuobara, 2014), and is also visible at a coastal Hi-net station (MURH).
159 This peak is small at inland Hi-net stations (KTGH and UMJF), and shifted to 0.2 Hz,
160 which is the secondary microseism peak that is commonly observed at many stations
161 and in a standard noise model (Peterson, 1993). Below 0.1 Hz, the DAS noise levels
162 appear to be worse than the DONET2 noise levels. At ~ 0.05 Hz, the DAS noise levels
163 also appear to be worse than the Hi-net noise levels after the instrument response
164 correction, although they are lower at ~ 0.01 Hz. Moreover, DAS recorded similar peaks
165 responsible to infragravity waves at ~ 0.02 Hz. We therefore expect our DAS
166 observations to be qualitatively similar to the DONET2 observations above 0.01 Hz.
167

168 **Example earthquake observations**

169 Our DAS observations recorded many earthquakes, despite relatively inactive regional
170 seismicity (Figure 1). Figure 3 shows three examples of observed earthquake signals.

171 One of the most clearly recorded events was a M2.9 earthquake that occurred ~100 km
172 from the cable. Figure 3a shows a comparison of the strain records at three channels,
173 with each consisting of the integrated strain rate after bandpass filtering at 2–16 Hz.

174 Both tiny P waves and large S waves are visible in most of the channels (Figure 3d),
175 with the exceptions being the uncoupled channels with small signal levels, as suggested
176 from the differences in the ambient standard deviation of the strain rate (Figure S1). The
177 maximum signal amplitudes were ~10 to 50 nanostrain, with large variations among the
178 channels. This large variation highlights the need to characterize each channel response

179 when conducting a quantitative analysis of these signals. The maximum amplitudes for
180 the same event that were recorded at two DONET2 stations, MRA04 and MRG29, were
181 ~50 and ~10 $\mu\text{m/s}$, which were located at epicentral distances of 56 and 131 km,

182 respectively. A relation between the 10–50 nanostrain DAS observations and 10–50

183 $\mu\text{m/s}$ ocean-bottom seismometer observation is explicable by assuming plane waves at a

184 velocity of the order of 1 km/s, which is expected from Figure 2.

185 The smallest earthquake recorded during these temporary observations was a M1.1
186 event that occurred 30–50 km from the cable (Figure 3b). The signal was only visible at
187 the channels with good coupling. Nevertheless, the signal-to-noise ratio was comparable
188 with that of a nearby Hi-net station (MURH) at some channels. This similarity likely
189 occurred because the dominant frequency of this event was 2–4 Hz, affected by the
190 attenuation effects along the propagation path, whereas the coastal Hi-net station had
191 relatively high noise levels in this frequency range.

192 The maximum earthquake we observed was a large teleseismic Mw7.7 earthquake that
193 occurred near Cuba on January 28, 2020 (Figure 3c). The signal was not visible at high
194 frequencies, but was clearly visible in the spectrograms below the microseism level at
195 most of the channels (Figure S2). The surface waves were detectable for ~1 hour;
196 however, the noise level was not good compared with the broadband seismometers, and
197 even worse than the response-corrected Hi-net records. The amplitude differences
198 among the DAS channels were large; channel 1290, which often observed large
199 amplitudes at high frequencies, recorded small amplitudes at low frequencies. This

200 again highlights the need to estimate each channel response as a function of frequency.

201

202 **Quasi-static observations: Periodic variations and migrating events**

203 What can we observe using a DAS system at much lower frequencies? One may expect

204 that the DAS observations would detect the tidal strain due to solid earth and ocean

205 tides, since the DAS measures strain. Figure 4 shows the extremely low-frequency DAS

206 records, with the mean strain rate measured at a 5-min interval over the entire

207 observation period for all of the channels along the cable. We observed large spatial and

208 temporal variations in the average strain rate above channel 1000. The observed

209 variation at channels 1000–4000 exhibited a nearly daily cycle with an amplitude on the

210 order of 0.1 nanostrain/s (10^{-10} strain/s); this is very large since the tidal deformation of

211 the Earth's surface is on the order of 10^{-12} strain/s. Noticeable variations were observed

212 at channels 4000–8000, where the cable passes the Tosabae Ridge, and similar but

213 smaller amplitude changes occurred above channel 8000. Temporal integration yields

214 strain variations of >20 microstrain, which cannot be explained by tidal deformation.

215 Nevertheless, the spectrum of these changes shows clear peaks that correspond to

216 diurnal and semidiurnal tidal periods (Figure S3). The very large change at around
217 channel 6000 has a clear 12.4-hour peak, which corresponds to the M2 constituent of
218 the tidal signal. Therefore, these variations are obviously controlled by ocean tides.

219 The rapid change in strain rate migrated a long distance along the cable above channel
220 4000. Some large migrations of a positive anomaly propagated ~10 km (2000 channels)
221 in ~6 hours, and many small-scale migrations occurred repeatedly across many of the
222 channels. The migration direction appears to be related to the geometry of the cable.

223 Each of the positive anomalies propagated from the lower to higher elevations on both
224 sides of Tosabae Ridge. Some large migrations, such as the events during the afternoon
225 of January 28th and on the morning of January 29th, propagated over the summit of the
226 ridge and continued further southward. The negative anomaly also migrated, but the
227 migration speed was variable and behaved more randomly than those of the positive
228 anomalies, which suggests that antisymmetric mechanisms influence the strain rate.

229 Although we have explained this change as a strain rate, the observed deformation is
230 likely not an actual physical variation in the length of the fiber-optic cable, but rather a
231 change in the refractive index of the fiber-optic cable due to variations in the ocean-

232 bottom water temperature. The observed strain ϵ depends on the temperature T ,

233 thermal expansion coefficient α , and change in the refractive index dn/dT as:

234
$$\frac{d\epsilon}{dT} = n\alpha + \frac{dn}{dT}.$$

235 Typical value of n , α , and dn/dT are 1.4, 4×10^{-7} , and 10^{-5} , respectively, which

236 means that dn/dT is the dominant term. $d\epsilon/dT$ has been measured $\sim 10^{-5}$ in

237 laboratory experiments (Hocker, 1979; Zumberge et al., 2018). We note that the real

238 coefficient may be small in the ocean-bottom environment, as estimated by Zumberge et

239 al. (2018), such that the degree of the temperature change described below may up to 3–

240 5 times larger. Nevertheless, we assume $dn/dT = 10^{-5}$ in our calculations, which

241 converts the apparent strain rate changes of 1 and 10 microstrain to 0.1 and 1 K

242 temperature changes for the basin (channels 1000–4000) and ridge (channels 4000–

243 8000) sections, respectively.

244 Temperature variations of ~ 0.2 K were measured by the temperature sensors of the

245 ocean-bottom pressure gauges along the Muroto cable (Inazu and Hino, 2011), which is

246 comparable with our observations in the basin section. However, we are unaware of any

247 direct measurements of ocean-bottom temperature changes that are as large as several

248 degrees. Conductivity-temperature-depth measurements have suggested large standard
249 deviations in the water temperature of up to several degrees at several locations near our
250 cable in the Nankai subduction zone (Watanabe and Uchida, 2016). The variations at
251 <800 m depth are particularly large and likely due to the effect of the Kuroshio Current;
252 our observations are likely related to such large variations.

253 These temperature variations must reflect the movement of ocean water, with the rapid
254 changes also suggesting movement at a sharp boundary between two water masses with
255 different temperatures. Although tidal modulation likely has a major influence on this
256 movement, the effect of the Kuroshio Current, a strong surface ocean current that flows
257 from west to east at >1 m/s across the study region, may not be negligible. The overall
258 orientation of the cable is at a large angle relative to the mean direction of the Kuroshio
259 Current, such that the influence of this current on the DAS observations may be
260 reduced. Nevertheless, the current direction near the ocean bottom might be different
261 due to the complex bathymetry of the region, including Muroto Basin and Tosabae
262 Ridge, which forms a narrow saddleback structure along the cable. Therefore, the
263 ocean-bottom water mass likely moves as a result of complex interactions between

264 relative steady ocean currents and quasi-periodic oceanic tides that are bounded by an
265 irregular bathymetry. It should be noted that the migration velocity of 10 km/6 hour
266 (~0.5 m/s) is only the apparent velocity along the cable orientation, such that the speed
267 of two- or three-dimensional boundaries can be much slower and yield a similar
268 apparent migration velocity. Nevertheless, this rapid, long-distance migration suggests
269 the existence of relatively large-scale movement near the deep (~1000 m) ocean bottom
270 at a velocity comparable with the Kuroshio Current at the surface. This observation may
271 prove useful in advancing our understanding of the mechanisms that drive the tidal
272 mixing of deep ocean water.

273

274 **Discussion and Conclusion**

275 We demonstrate that DAS can observe a suite of geophysical signals via DAS
276 observations from an unused seafloor fiber-optic cable offshore Cape Muroto over a
277 five-day period. Our original interest was broadband seismic signals since the measured
278 quantity is supposed to be the axial strain of the cable. We show that the performance of
279 high-frequency (>1 Hz) seismic observations is almost comparable with those of ocean-

280 bottom permanent seismic stations, as long as the cable is well-coupled with the ocean
281 bottom. Although only one component of the strain is measurable, high-density DAS
282 observations at many channels could prove useful for quantifying different aspects of
283 the local seismic structure and seismic source parameters.

284 The Nankai subduction zone is well-known for various slow earthquake activity.

285 Although our temporary observations did not detect any tectonic tremor or low-
286 frequency earthquakes, which generally yields signals above 1 Hz, the noise level
287 suggests that the cable has the ability to detect these phenomena if they occur within a
288 few tens of kilometers of the cable. However, in the frequency range for very low
289 frequency earthquakes, i.e., 0.02-0.05 Hz, the DAS observations are noisier than the
290 short-period sensors, which makes such event detection impossible unless they occur
291 very close to the cable.

292 The major noise source for the DAS measurements is the noise due to temperature-
293 dependent changes in the refractive index; this effect is particularly large at very low
294 frequencies. The amplitude of the temperature-dependent noise is as much as 10
295 microstrain for quasi-static (>5 min) observations, which is about two orders of

296 magnitude larger than expected for earth and ocean tide signals. However, this
297 temperature-dependent noise can be used as a signal to monitor the temperature field if
298 the temperature varies systematically in space and time, as observed in our experiment.
299 This strain-to-temperature conversion is only possible via continuous spatiotemporal
300 monitoring, such as DAS observations. We can identify several migration sequences of
301 rapid temperature changes that are up to several degrees, some of which propagated
302 more than 10 km over several hours. We believe that this is the first report of such
303 ocean-bottom temperature migration events. These events likely arise from interactions
304 between the periodic tides, complex bathymetry, and strong Kuroshio Current, and may
305 contribute to deep-water mixing processes near the ocean bottom.

306

307 **Declarations**

308 **The authors *must* provide the following sections under the heading “Declarations”.**

309 **Ethics approval and consent to participate**

310 Not applicable.

311 **Consent for publication**

312 Not applicable.

313 **List of abbreviations**

314 DAS: Distributed Acoustic Sensing.

315 JAMSTEC: Japan Agency for Marine Earth Science and Technology

316 **Availability of data and materials**

317 All data necessary to make figures will be provided upon the request to
318 the authors.

319 **Competing interests**

320 We have no financial and non-financial competing interests.

321 **Funding**

322 This research was supported by JSPS Kakenhi (16H02219), MEXT
323 Kakenhi (16H06477), and the Earthquake and Volcano Hazards
324 Observation and Research Program of MEXT.

325 **Authors' contributions**

326 S.I. analyzed DAS data and wrote most of the manuscript. E.A and H.M.
327 carried out DAS observation. E.A. pointed out the importance of
328 temperature. All authors contributed to finalize the manuscript.

329 **Acknowledgements**

330 We used The Generic Mapping Tool (Wessel et al., 2013) to prepare
331 figures.

332 **Authors' information**

333 S.I. is a professor in Department of Earth and Planetary Science, The
334 University of Tokyo. E.A. and H.M. are senior researcher and researcher
335 in Japan Agency for Marine Earth Science and Technology.

336

337 **References**

338 Ajo-Franklin, J. B., Dou, S., Lindsey, N. J., Monga, I., Tracy, C., Robertson, M.,
339 Tribaldos, V. R., Ulrich, C., Freifeld, B., Daley, T., Li, X. (2019) Distributed acoustic
340 sensing using dark fiber for near-surface characterization and broadband seismic event
341 detection. Scientific Reports 9:1328. doi:10.1038/s41598-018-36675-8
342 Araki, E., Shinohara, M., Sacks, S., Linde, A., Kanazawa, T., Shiobara, H., Mikada, H.,
343 Suyehiro, K. (2004) Improvement of seismic observation in the ocean by use of seafloor
344 boreholes. Bull. Seismol. Soc. Am. 94:678-90.

345 Benioff, H. (1935) A linear strain seismograph. *Bull. Seismol. Soc. Am.* 25: 283-309.

346 Beroza, G. C., Ide, S. (2011) Slow earthquakes and nonvolcanic tremor. *Annual review*
347 *of Earth and Planetary Sciences* 39:271-296. doi:10.1146/annurev-earth-040809-152531

348 Hartog, A. (2017) *An introduction to distributed optical fibre sensors*. Boca Raton, FL:
349 CRC Press.

350 Hocker, G. B. (1979) Fiber-optic sensing of pressure and temperature. *Applied Optics*
351 18:1445-1448.

352 Inazu, D., Hino, R. (2011) Temperature correction and usefulness of ocean bottom
353 pressure data from cabled seafloor observatories around Japan for analyses of tsunamis,
354 ocean tides, and low-frequency geophysical phenomena. *Earth Planet Space* 63:1133-
355 1149. doi:10.5047/eps.2011.07.014

356 Lindsey, N. J., Martin, E. R., Dreger, D. S., Freifeld, B., Cole, S., James, S. R., Biondi,
357 B. L., Ajo-Franklin, J. B. (2017) Fiber-optic network observations of earthquake
358 wavefields. *Geophysical Research Letters* 44:11-792. doi:10.1002/2017GL075722

359 Lindsey, N. J., Rademacher, H., Ajo-Franklin, J. B. (2020) On the broadband
360 instrument response of fiber-optic DAS arrays. *Journal of Geophysical Research: Solid*

361 Earth 125:e2019JB018145. doi:10.1029/2019JB018145

362 Momma, H. Fujiwara, N., Kawaguchi, m K., Iwase, R., Suzuki, S., Kinoshita, H. (1997)

363 Monitoring system for submarine earthquakes and deep sea environment. Proc.

364 MTS/IEEE OCEANS '97 2:1453-1459.

365 Obara, K., Kato, A. (2016) Connecting slow earthquakes to huge earthquakes. Science

366 353:253-257. doi:10.1126/science.aaf1512

367 Peterson, J. (1993) Observations and modeling of seismic background noise. US

368 Geological Survey Open-File Report 93-322.

369 Shinohara, M., Yamada, T., Akuhara, T., Mochizuki, K., Sakai, S., Hamakawa, M.,

370 Kasajima, T., Arioka, T., Kubota, S. (2019) Distributed Acoustic Sensing measurement

371 by using seafloor optical fiber cable system off Sanriku for seismic observation. In

372 OCEANS 2019 MTS/IEEE SEATTLE (pp. 1–4). Seattle, WA: IEEE.

373 doi:10.23919/OCEANS40490.2019.8962757

374 Sladen, A., Rivet, D., Ampuero, J. P., De Barros, L., Hello, Y., Calbris, G., Lamare, P.

375 (2019) Distributed sensing of earthquakes and ocean-solid Earth interactions on seafloor

376 telecom cables. Nature communications 10:1-8. doi:10.1038/s41467-019-13793-z

377 Spica, Z. J., Perton, M., Martin, E. R., Beroza, G. C., Biondi, B. (2020a) Urban seismic
378 site characterization by fiber-optic seismology. *Journal of Geophysical Research: Solid*
379 *Earth* 125:e2019JB018656. doi:10.1029/2019JB018656

380 Spica, Z. J., Nishida, K., Akuhara, T., Pétrélis, F., Shinohara, M., Yamada, T. (2020b)
381 Marine sediment characterized by ocean-bottom fiber-optic seismology. *Geophysical*
382 *Research Letters* 47:e2020GL088360. doi:10.1029/2020GL088360

383 Suetsugu, D., Shiobara, H. (2014) Broadband ocean-bottom seismology. *Annu. Rev.*
384 *Earth Planet. Sci.* 42:27-43. doi:10.1146/annurev-earth-060313-054818

385 Wang, H. F., Zeng, X., Miller, D. E., Fratta, D., Feigl, K. L., Thurber, C. H., Mellors, R.
386 J. (2018) Ground motion response to an ML 4.3 earthquake using co-located distributed
387 acoustic sensing and seismometer arrays. *Geophysical Journal International* 213:2020-
388 2036. doi:10.1093/gji/ggy102

389 Watanabe, S., Uchida, T. (2016) Stable structures of temperature and salinity validated
390 by the repeated measurements in the few-miles-square regions off Japan coast in the
391 western Pacific. *Reports on Hydrographic Oceanography Research*,53:57-81.

392 Wessel, P., Smith, W. H. F., Scharroo, R., Luis, J., Wobbe, F. (2013) *Generic Mapping*

393 Tools: Improved Version Released. EOS Trans. AGU 94:409-410, 2013.

394 doi:10.1002/2013EO450001

395 Williams, E. F., Fernández-Ruiz, M. R., Magalhaes, R., Vanthillo, R., Zhan, Z.,

396 González-Herráez, M., Martins, H. F. (2019) Distributed sensing of microseisms and

397 teleseisms with submarine dark fibers. Nature Communications 10:1–11.

398 doi:10.1038/s41467-019-13262-7

399 Yu, C., Zhan, Z., Lindsey, N. J., Ajo-Franklin, J. B., Robertson, M. (2019) The potential

400 of das in teleseismic studies: Insights from the Goldstone experiment. Geophysical

401 Research Letters 46:1320-1328. doi:10.1029/2018GL081195

402 Zhan, Z. (2020) Distributed acoustic sensing turns fiber-optic cables into sensitive

403 seismic antennas. Seismological Research Letters 91:1-15. doi:10.1785/0220190112

404 Zumberge, M. A., Hatfield, W., Wyatt, F. K. (2018) Measuring seafloor strain with an

405 optical fiber interferometer. Earth and Space Science 5:71-379.

406 doi:10.1029/2018EA000418

407

408

409 **Figure legends**

410 Figure 1. Locations of the seafloor fiber-optic cable and detected hypocenter
411 distribution during the observation period. The bold line represents the cable route of
412 the Comprehensive Seafloor Monitoring System off Cape Muroto, with the red section
413 indicating the 50-km-long DAS observation section. The two small open triangles along
414 the cable show the ocean-bottom seismometer locations. The triangles with different
415 colors are the stations that were used for a comparison with the DAS observations:
416 MURH and KTGh (Hi-net), UMJF (F-net), and MRA04 and MRG29 (DONET2). Red
417 circles indicate the epicenters of earthquakes that occurred during the January 27–31,
418 2020 (JST), period, as determined by the Japan Meteorological Agency.

419 Figure 2. Comparison of the noise levels between the DAS and nearby seismometers. a.
420 Strain rate spectra at ten selected channels. Each line shows the median value of the
421 periodograms calculated at 5-min intervals for the entire observation period (January
422 27–31, 2020 (JST)), which were computed at 5-min intervals during the entire
423 observation period (Figure S2). b. Acceleration spectra at five seismic stations. Solid
424 and dashed lines are for the vertical- and horizontal-component seismometers,

425 respectively. Bold gray lines show a standard noise model (Peterson, 1993). MRA04
426 and MRG29 are DONET2 stations, and UMJF is a F-net station; each of these stations
427 has a broadband sensor. We corrected the instrumental response for the MURH and
428 KTGH spectra, which are Hi-net stations.

429 Figure 3. Example earthquake signal observations. a. A moderate-sized (M2.9) event on
430 January 27, 2020, at 16:23:31.8 (UT). The observed strain at three DAS channels (top)
431 and the horizontal velocity seismograms at two DONET2 stations (bottom) are shown;
432 all of the waveforms have been bandpass filtered at 2–16 Hz. b. A very small (M1.1)
433 event on January 30, 2020, at 00:20:25.7 (UT). The observed strain at three DAS
434 channels (top) and the horizontal velocity seismograms at two Hi-net stations (bottom)
435 are shown; all of the waveforms have been bandpass filtered at 2–16 Hz. c. A
436 teleseismic Mw7.7 event on January 28, 2020, at 19:10:24 (UT) near Cuba. The
437 observed strain at three DAS channels (top), and the horizontal velocity seismograms at
438 a DONET station (MRG29) and F-net station (UMJF) (bottom) are shown; all of the
439 waveforms have been bandpass filtered at 0.01–0.1 Hz. All of the velocity data are
440 shown relative to the origin time of the event. d. DAS records for all of the channels and

441 the earthquake in a. The amplitudes are presented as the logarithm of the normalized
442 absolute amplitude of the strain rate, and have been bandpass filtered at 2–8 Hz.

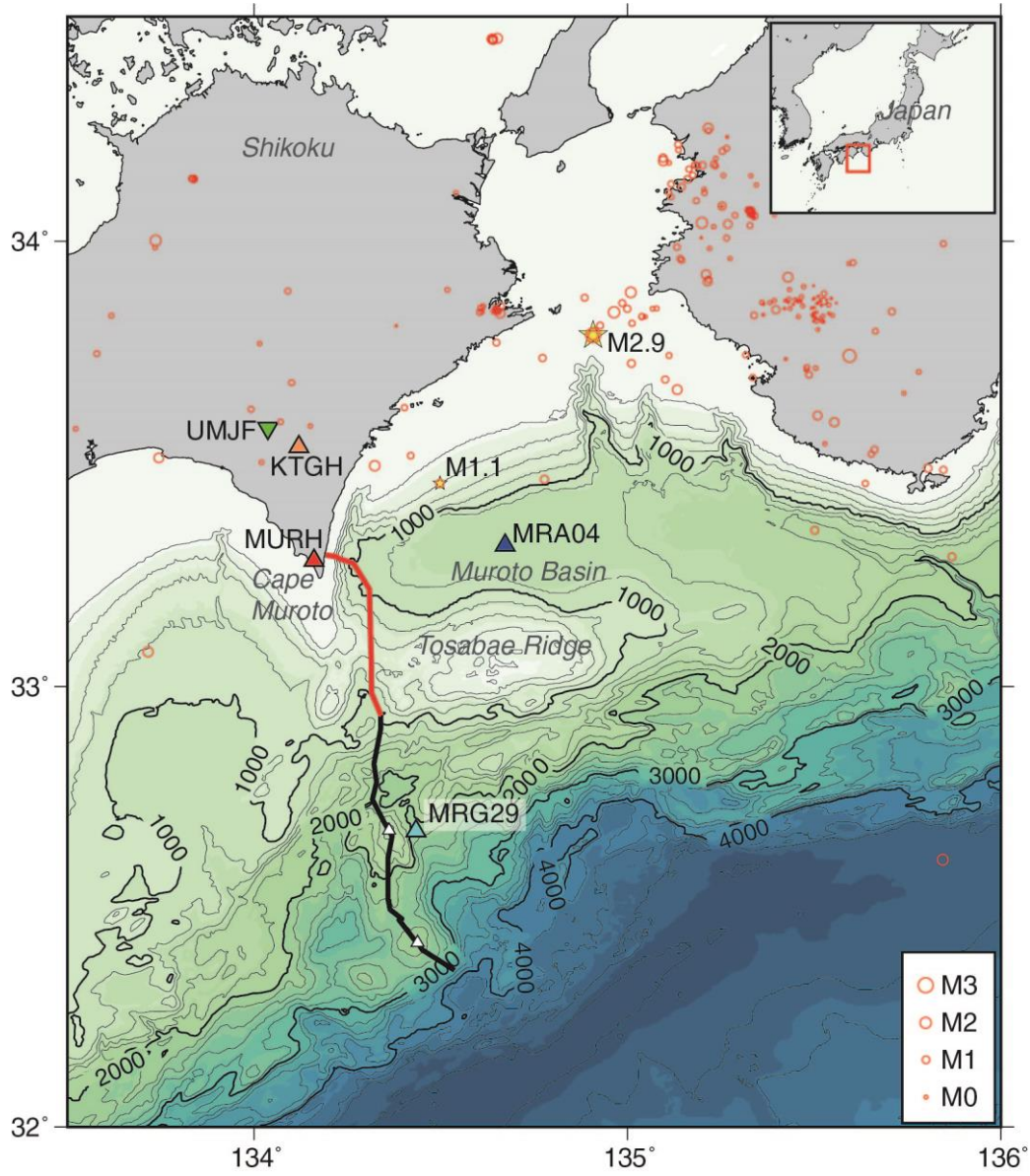
443 Figure 4. Five-minute averages of the spatial and temporal changes in strain rate for the
444 entire observation period. a. Bathymetry profile along the cable route. b. Space–time
445 plot of the average strain rate (5-min interval) for the entire observation period. c.
446 Temporal changes in the average strain rate (5-min interval) at three selected channels.
447 The traces have been shifted vertically for comparison. d. Integration of the strain rate
448 records shown in c.

449

450 **Additional Files**

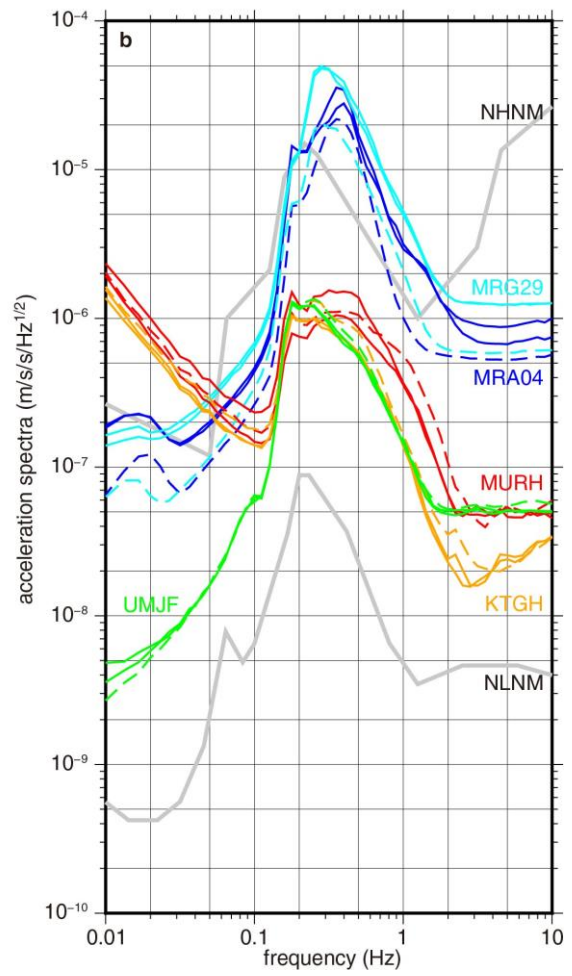
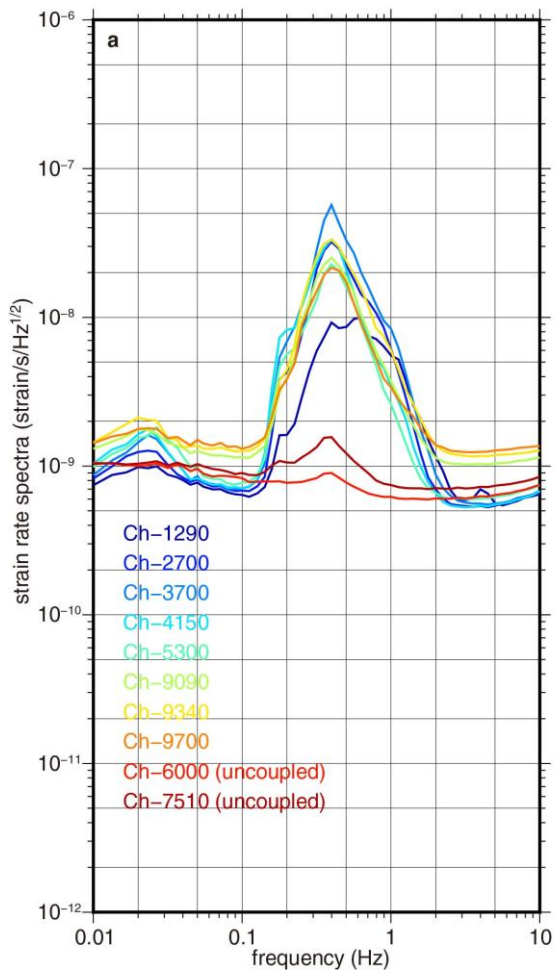
451 [Additional_file_1.pdf](#): A file containing three supplemental figures: Figures S1, S2, and
452 S3.

453



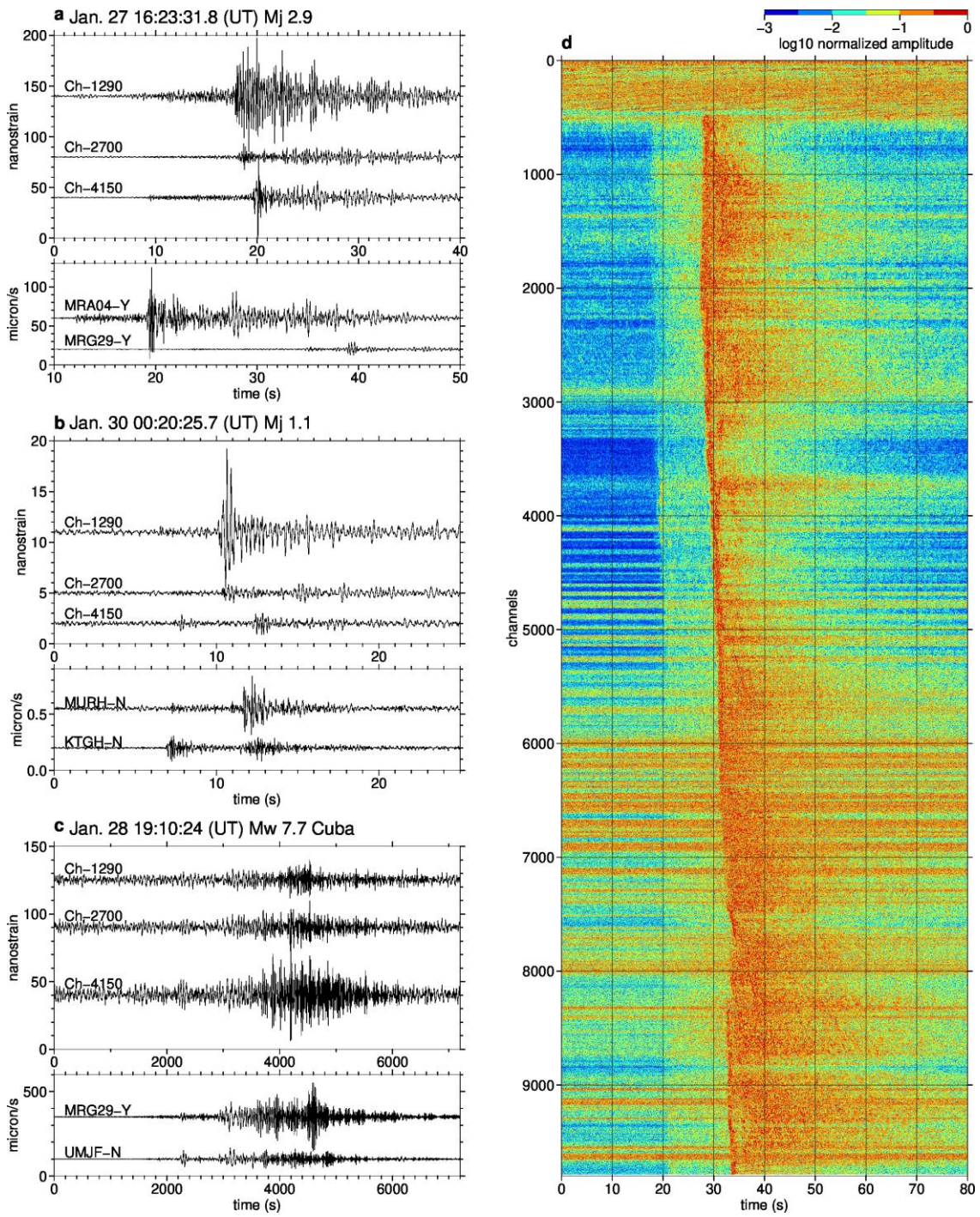
454

455 Figure 1



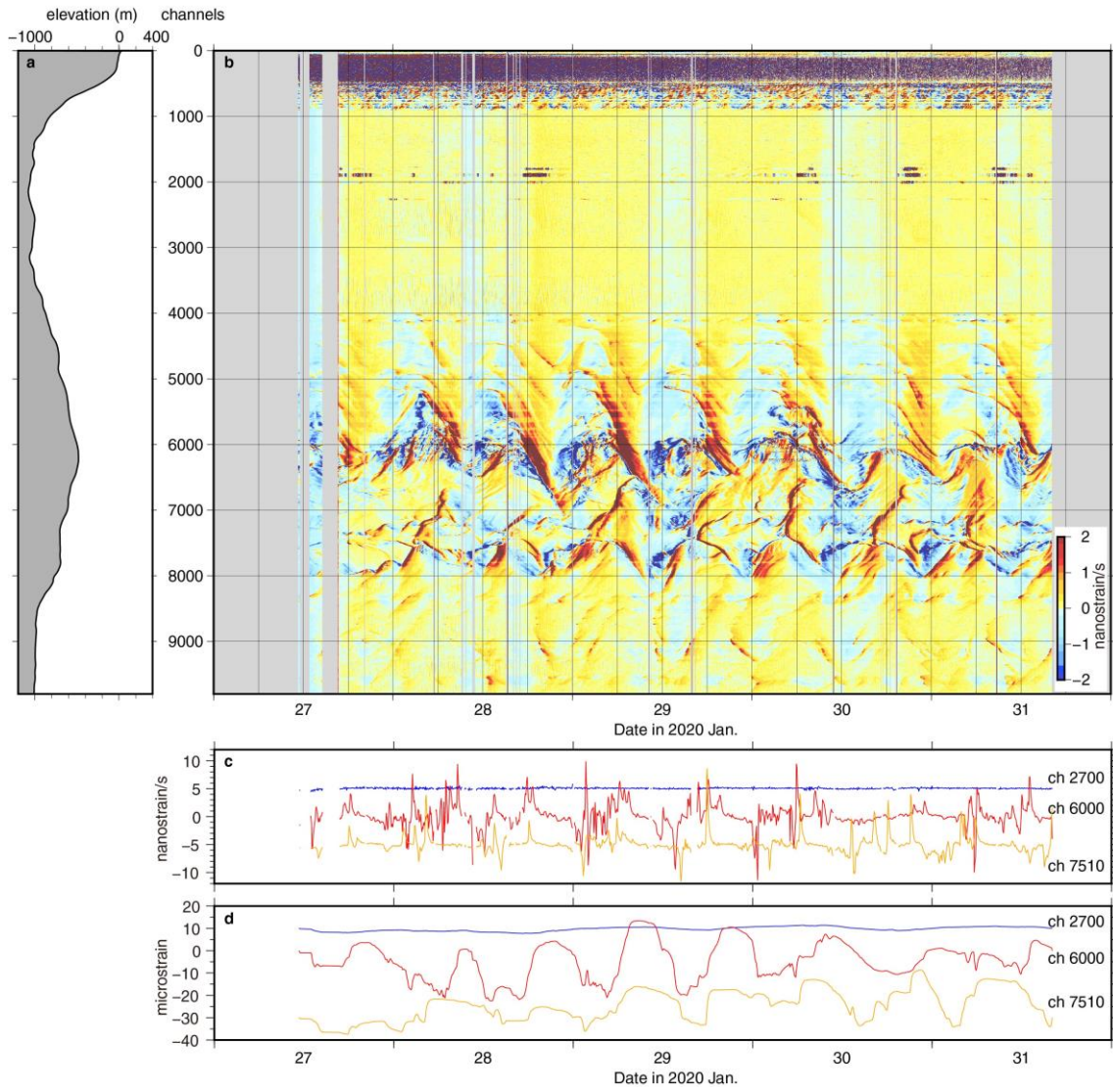
456

457 Figure 2



458

459 Figure 3



460

461 Figure 4

462